Retinal Image Analysis Using Convolutional Neural Network

Aderemi Olalekan Adesoji
x19116578@student.ncirl.ie
MSc. Data Analytics

Sunil Vimala Raghunatharaju
x19148208@student.ncirl.ie
MSc. Data Analytics

Devvrat Parihar
x19191855@student.ncirl.ie
MSc. Data Analytics

***Abstract*—Retinal Optical Coherence Tomography (OCT) involves the imaging of the retina using low-coherence light. The analysis of these images for eye defects is commonly referred to as Retinal Image Analysis (RIA). There are numerous demands for retinal analysis to be more accurate, reliable, and measurable. This project applies Convolutional Neural Network (CNN) to predict the presence of Choroidal Neovascularisation (CNV), Diabetic Macular Edema (DME) and Drusen in OCT images. The model was applied to an image dataset consisting of over 84000 pre-labelled images. The OCT images were pre-processed by resampling using a random under sampler to handle the imbalance in classes. Image generation was used to feed batches of randomly generated images, based on the original images from the dataset, to the CNN classification algorithm. The model produced relatively high sensitivity (recall) scores for each class in the model; all above 0.9. The F1 score was used as a more generalised performance metric as it balances the trade-off between precision and recall scores. The F1 score for the classes ranged between 0.93 and 1.00.**

***Keywords*—Choroidal Neovascularisation (CNV), Diabetic Macular Edema (DME), Drusen, Convolutional Neural Network**

I. INTRODUCTION

The retina is a multi-layer cartilage filling the inside of the eye which allows the transformation of light rays into synaptic signals ideal for further processing in the brain's cerebral cortex; hence it is a branch of the brain. Based on this eye-brain architecture, both eye disorders, as well as disorders that influence blood flow around the brain, may show up in the retina. These include ophthalmic disorders such as macular degeneration, diabetic retinopathy, and glaucoma which are the three of the most severe causes of blindness in the developed world, among middle-aged people - with diabetic retinopathy being the leading cause of blindness in middle-aged people [1].

Consequently, while the retina is susceptible to organ-specific and infectious ailments, on the flip side, the examination of the retina makes it easier to identify, treat and handle disorders of the eye, symptoms of diabetes, hypertension and other heart conditions. Early detection and prompt treatment are said to reduce vision impairment in diabetic patients [2].

The three eye defects discussed in this paper are:

1) Choroidal Neovascularisation (CNV):

This specific ocular deficiency arises when new blood vessels are developed in the choroid layer of the eye. This condition occurs in individuals with defects in the innermost layer of the choroid, also called the Bruch membrane, and is often worsened by deep myopia, malignant myopic deterioration and age-related changes [3].

2) Diabetic Macular Edema (DME)

This is a diabetes mellitus complication where the hyperglycaemia damages the retinal vessel walls leading to a breakdown of the blood-retinal barrier which in turn causes fluid leakage and damage to photoreceptors in the eyes; this condition is most common in patients with type 2 diabetes [4].

3) Drusen

Drusen are concentrations of flakes that appear as relatively small yellow or white particles that build up between the membrane of Bruch and the epithelium tissue, predominantly found in middle-aged normal eyes and eyes with age-related macular degeneration [5].

To detect these ocular defects, ophthalmologists study the individual layers of Retinal Optical Coherence Tomography Images, commonly known as OCT, for the presence of anomalies. OCT is the imaging of cross-sections of the retina using low-coherence light waves. This process of studying OCT images is widely referred to as Retinal Image Analysis (RIA).

With the advent of technology, Retinal Image Analysis has become widely automated. One of the earliest implementations of RIA was by documented by [6] in 1984 on the detection of microaneurysms in OCT images. In the 1990s, there was a significant shift with the introduction of digital retinal imaging and the growth of electronic filter-based imaging techniques. These innovations gave rise to an ever-increasing number of articles published in this area. Digital RIA has enormous potential as there is the demand for a retinal assessment to be more accurate, reliable, and more measurable. The daily costs of eye care clinicians' assessments and the ever-increasing number of retinal images to be examined are primary factors for this project research. With this application, clinical professionals will have access to quicker analysis of OCT images with reduced cost as opposed to manual identification of eye defects. The project uses CNN to detect and predict CVN, DME and Drusen in OCT images.

In subsequent sections of this report, a summary of similar reports is discussed in the literature review, detailing both positive and negative aspects of the report as well as limitations of discovered in those reports. The methodology discusses the technical details applied to answer the research question; the project applied the Knowledge Discovery in Databases (KDD) methodology throughout the implementation phase. The outcomes are detailed in the "Evaluation and Results" section of the report, discussing the implications of the discovery from the project. Finally,

a summary of all the findings, limitations and improvement areas are outlined in the "Conclusion" section of this report.

II. Related Work

An early application of ANN in the detection of diabetic retinopathy was by [7]. The author fed images of 20 x 20 pixels into a NN with 400 inputs. This method of classifying the entire pixel patches rather than using a pixel resolution classification produced an exudate detection sensitivity of over 90%. The limitation to this model, however, was the long training time; it took about 120 hours to train the model. A study by [8], applied a deep learning algorithm in the detection of Diabetic Retinopathy (DR) in fundus images. The dataset used include over 75000 fundus images in which a panel of ophthalmologists determined the ground truth for the dataset. The model produced a sensitivity and specificity both over 90% as well as an AUC of 0.97.

[9] applied feature selection and classification using multi-layered neural network classifier to classify diabetic retinopathy present in retinal images. The research measured sensitivity and specificity both over 90% accuracy. The model achieved such high performance without transforming the images to greyscale. This was done by applying Fuzzy C-Regression Model (FCM) colour segmentation, Genetic Algorithm (GA) based feature selection and Neural Network (NN) classifiers. While the results were impressive, the contact area between the detected exudates and fovea (the central macular region) was identified as an area defined for further analysis. [10] also applied Fuzzy C-means (FCM) clustering for the segmentation of bright regions in the images while an SVM was used to detect if said regions were hard exudates or not. On the other hand, [11] applied Support Vector Machine (SVM) classifier to build a model to predict the presence of Hard Exudates and Haemorrhage in retinal images which are both somewhat common eye defects. The model achieved an accuracy of 96% and 85% respectively. A related methodology was applied by [12], where the FCM clustering was also used to segment retinal images while an artificial neural network classifier was used for classification. The proposed model was evaluated using sensitivity and specificity, scoring 95% and 89% respectively, in the identification of retinopathy.

A research carried out in 2018 by [13] proposed a method to detect CNV in 42 spectral-domain OCT images. The model utilised 7 grey-level features, 3 spatial features, and 14 layer-like features to train the neural network classifier. As a process to ease identification of the layers in the retinal images based on the different thicknesses, the authors introduced multi-scale bright and dark layer detection filters. Finally, they detected retinal surfaces using a constrained graph search algorithm, resulting in a method that outperformed other methods in similar domain [13]. Their implementation of Non-negative Conjugate Gradient (NNCG) algorithm surpassed the performance of the Non-networked Microgrids (NNMG) algorithm resulting from the enhancement of the ellipsoid zone using bright layer detection filter. One limitation encountered in this project was the restriction of surface detection accuracy in layers resulting from the low contrast between the multiple layers making their boundaries nearly invisible. Another limitation listed was the high computing time required to implement the algorithm.

In [14], the authors examined 3 neural network classifiers: Support Vector Machine (SVM), Radial Basis Function (RBF) and Multilayer Perceptron (MLP) in the detection of hard exudates in fundus images. The authors adopted 2 criteria for the detection: lesion-based and image-based. As part of the pre-processing steps, the authors performed colour normalisation and luminosity to increase the contrast between the image background and the exudates. Next, they segmented the image to the detection of the exudates easier for the machine. As a final step before classification, certain features were extracted based on the traits used by ophthalmologists to visually differentiate between exudates and other retinal formations. The authors assessed the performance of their model using the positive predictive value (PPV) and sensitivity (SE). For the lesion-based approach, the model achieved an SE and PPV of 88% and 80% respectively for the MLP, 88.49% and 77.41% for the RBF, and 87.61% and 83.51% for the SVM. The specificity, sensitivity, and accuracy were measured for the image-based approach. The MLP achieved the best result with a specificity, sensitivity, and accuracy of 92.59%, 100% and 97.01% respectively. All the other classifiers also performed well but not as good as the MLP classifier.

Alternatively, a less common approach was adopted by [15]. The algorithm was based on Fisher's linear discriminant analysis and performs classification using colour information. The algorithm used a linear combination of features to classify more than 2 classes of objects. The proposed algorithm achieved a sensitivity of 88%. In a bid to segment optic disc and retinal vasculature, [16] carried out pre-processing by first normalising OCT images and then trained a CNN model with an accuracy of 92% of the ground truths.

[17] trained an 18-layer convolutional neural network on over 1400 fundus images to classify if the retinal images are normal or glaucomic. The author extracted the Cup to Disc Ratio (CDR) as its basis for classifying the images. The model achieved a sensitivity and specificity both around 98%. On the other hand, [18], [19] both applied the Support Vector Machine (SVM) classifier for the detection of glaucoma. While their models were based on different features namely HOS and discrete wavelet transform, and Gabor transform-based features, respectively, both models performed similarly in terms of specificity. However, [19] performed better in terms of sensitivity, scoring 93%.

[20] proposed the use of a six-layered deep convolutional neural network. The authors applied data augmentation to supplement for the less-than-adequate size of the data set. They also applied the dropout regularisation to enhance the performance of the detection and classification. The results of the model measured using the Area Under Curve (AUC) were 0.887 and 0.831 for the 2 datasets where the model was applied. Three independent studies, [21]–[23], applied the k-Nearest Neighbour (kNN) on different sizes of fundus images using different feature selection methods. [23] used the local configuration pattern

to extract features from the microstructures of images, otherwise known as textons. Feature selection and ranking was performed using sequential floating forward search. The model attained a 95% accuracy upon completion, which was the highest performance amongst the 3 models.

III. Data Mining Methodology

The choice of dataset was gotten from Mendeley Data Repository [24]. The dataset is prelabelled as either CNV, DME, Drusen or Normal and further divided into training and testing categories. The number of images in the dataset is shown in Table 1 below.

The entire program was written in python using the jupyter notebook and executed using a system configuration of Intel Core i5 8th gen CPU, 8GB RAM with GPU.

Table 1: Dataset breakdown

Train	
CNV	37205
DME	11348
Drusen	8616
Normal	26315
Total	**83484**
Test	
CNV	250
DME	250
Drusen	250
Normal	250
Total	**1000**

```
X_train, Y_train = next(train_data_gen)
X_test, Y_test = next(test_generator)
print(X_train.shape)
```

```
(76716, 128, 128, 3)
```

Figure 1: Image Characteristics

The images are multichannel images having 128*128 pixels each as shown in Figure 1. A snapshot of the original images for each class from the dataset can be found below in Figure 2 - Figure 5.

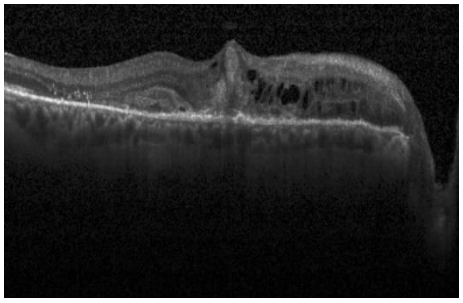

Figure 2:CNV

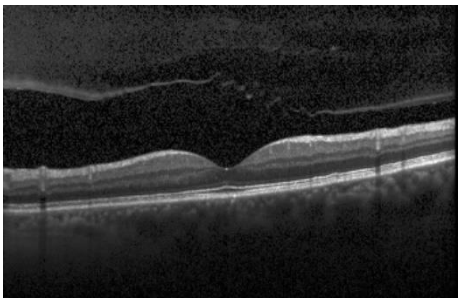

Figure 3: DME

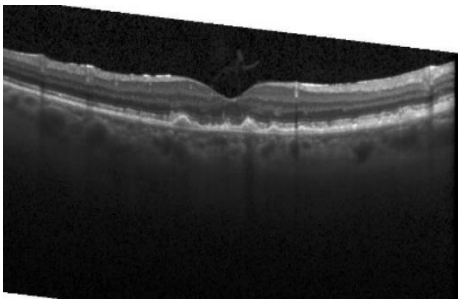

Figure 4: Drusen

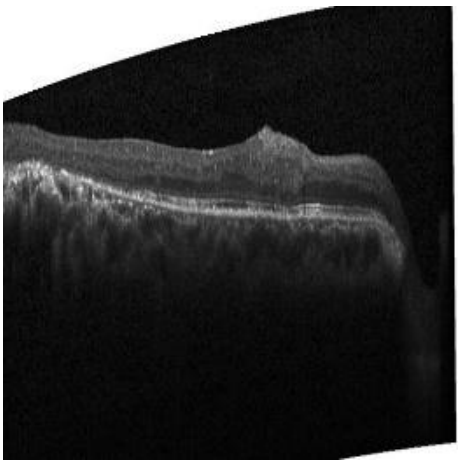

Figure 5: Normal

The chosen deep learning classifier was the convolutional neural network algorithm. CNNs are often referred to as regularised multilayer perceptrons. While typical multilayer perceptrons have each node or neuron in one layer connecting to all the nodes in the following layer, this full connected feature makes these types of networks susceptible to overfitting. CNN handles this using the ranked pattern in data to assign weights to loss functions and then compiles convoluted patterns from smaller patterns. This makes CNN suitable for the classification problem posed in this project.

The process begins by feeding the image as an input into the algorithm. Features are then learned from patterns in the image using the Rectified Linear Unit (ReLU) activation function. This function transforms the summed weighted input from the node to activate the said node or as a resultant output for that input. The ReLU function outputs the input directly if it is positive, otherwise, it sends an output of 0 [25]. A layer of batch normalisation is applied to standardise the inputs to a layer for each mini batch. It is applied directly

to the inputs from the layer and the activations from prior layers. The batch normalisation layer reduces the number of epochs needed to train the model thus stabilising the learning process and reducing the training time. The result from this is then passed into the pooling layer. The pooling layers offer an alternative to map sampling functions by summarizing the position of features in the feature map patches. The two pooling strategies applied during this project are the average pooling and the max pooling, which describe the average position of the feature and the most prominent position of the feature.

The choice of optimisation algorithm was the Adam optimisation algorithm. This was used over the traditional stochastic gradient descent approach to update the network weights in the training data.

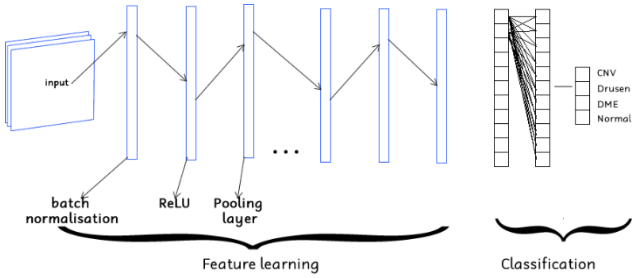

Figure 6: Convolutional Neural Network Layout

The "ImageDataGenerator" function in Keras was used to perform data augmentation on-the-fly during training. This works by first accepting a batch of images from the original dataset as the input, the function then transforms the batch of images using a number of randomised rotations while retaining the original class label. The returned value from this function is only the transformed batch of the images generated from the function. This is finally passed to the CNN to train the model. This entire process is done at training time. The figure below shows an overview of the process carried out by the imagedatagenerator function.

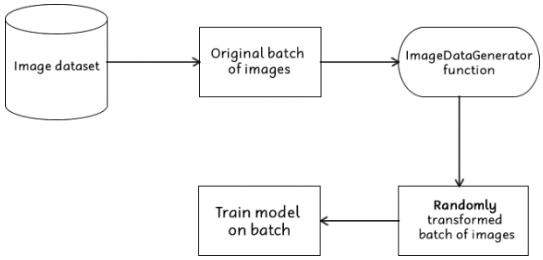

Figure 7: ImageDataGenerator procedure

To instantiate the tuner, the hyperband algorithm was used for the hyperparameter search. A subset of the original dataset, different from the subset used for training and testing, was used for the hyperparameter tuning. Each model was trained for at most 8 epochs, and two iterations of the Hyperband algorithm was run. Afterwards, the best models found during the search was then retrieved using the get_best_models function. Finally, the model was then built using the optimum parameter values found by the search. The dataset is split into 3 sections namely the training set, validation set, and the test set. Random under sampling involves randomly eliminating samples from the majority class. This under sampling technique was applied to the training dataset. While this option is not always advised, the number of images produced was sufficient enough for the training which would ordinarily be computationally heavy given large size of data.

The validation set is essential as it gives allowance for the exploration of different model architectures. If the same batch of data is used for any 2 of these sets, there is a possibility of overfitting the model to a particular set thus missing the ability to calculate the performance of the model on unseen data, often referred to as data leakage. It is worth noting that separate datasets were used for validation set, training set, and testing set.

The proposed system is represented in Figure 8. It represents a graphical overview of the steps involved in the detection and classification of an eye defect using the proposed model.

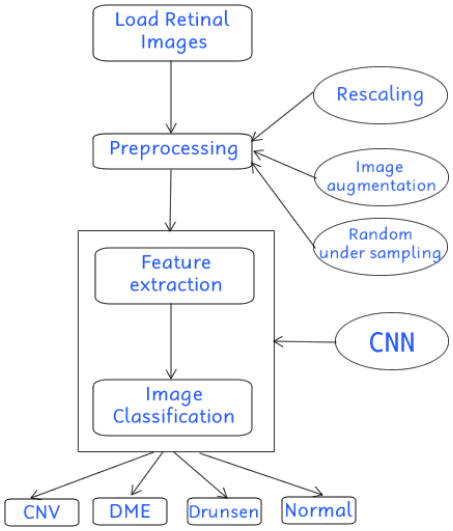

Figure 8: Proposed Eye Defect Detection System

The measure the preliminary performance of the validation and training sets on the model, the accuracy and loss functions were used. The image below shows how the increase with relation to the number of epochs while the loss reduces for the corresponding number of epochs.

```
Trial complete
Trial summary
|-Trial ID: c9e7c2c1857f9ed09554be99246f7f39
|-Score: 0.9375
|-Best step: 0
Hyperparameters:
|-conv_blocks: 5
|-dense_activation: relu
|-dropout: 0.1
|-filters_0: 96
|-filters_1: 96
|-filters_2: 224
|-filters_3: 96
|-filters_4: 160
|-hidden_size: 40
|-learning_rate: 0.00035515842891719766
|-pooling_0: avg
|-pooling_1: avg
|-pooling_2: max
|-pooling_3: max
|-pooling_4: avg
|-tuner/bracket: 1
|-tuner/epochs: 8
|-tuner/initial_epoch: 3
|-tuner/round: 1
|-tuner/trial_id: 74dd6c44d249868f3cf36d987f7d9411
```

Figure 9: Optimum hyperparameter obtained

The image above shows a snapshot of the optimum parameters derived from the hyperparameter tuning for the model. Some of the parameters include the learning rate, and the pooling layer.

The learning rate controls the rate of change of the model in response to the calculated error after each iteration where the weights are updated while the pooling layers offer an alternative to map sampling functions by summarizing the position of features in the feature map patches.

Layer (type)	Output Shape	Param #
input_1 (InputLayer)	[(None, 128, 128, 3)]	0
conv2d (Conv2D)	(None, 128, 128, 96)	4416
batch_normalization (BatchNo	(None, 128, 128, 96)	384
re_lu (ReLU)	(None, 128, 128, 96)	0
conv2d_1 (Conv2D)	(None, 128, 128, 96)	138336
batch_normalization_1 (Batch	(None, 128, 128, 96)	384
re_lu_1 (ReLU)	(None, 128, 128, 96)	0
average_pooling2d (AveragePo	(None, 64, 64, 96)	0
conv2d_2 (Conv2D)	(None, 64, 64, 96)	138336
batch_normalization_2 (Batch	(None, 64, 64, 96)	384
re_lu_2 (ReLU)	(None, 64, 64, 96)	0
conv2d_3 (Conv2D)	(None, 64, 64, 96)	138336
batch_normalization_3 (Batch	(None, 64, 64, 96)	384
re_lu_3 (ReLU)	(None, 64, 64, 96)	0
max_pooling2d (MaxPooling2D)	(None, 32, 32, 96)	0
conv2d_4 (Conv2D)	(None, 32, 32, 64)	92224
batch_normalization_4 (Batch	(None, 32, 32, 64)	256
re_lu_4 (ReLU)	(None, 32, 32, 64)	0
conv2d_5 (Conv2D)	(None, 32, 32, 64)	61504
batch_normalization_5 (Batch	(None, 32, 32, 64)	256
re_lu_5 (ReLU)	(None, 32, 32, 64)	0
max_pooling2d_1 (MaxPooling2	(None, 16, 16, 64)	0

Figure 10: Model Summary

conv2d_6 (Conv2D)	(None, 16, 16, 128)	123008
batch_normalization_6 (Batch	(None, 16, 16, 128)	512
re_lu_6 (ReLU)	(None, 16, 16, 128)	0
conv2d_7 (Conv2D)	(None, 16, 16, 128)	245888
batch_normalization_7 (Batch	(None, 16, 16, 128)	512
re_lu_7 (ReLU)	(None, 16, 16, 128)	0
max_pooling2d_2 (MaxPooling2	(None, 8, 8, 128)	0
conv2d_8 (Conv2D)	(None, 8, 8, 160)	307360
batch_normalization_8 (Batch	(None, 8, 8, 160)	640
re_lu_8 (ReLU)	(None, 8, 8, 160)	0
conv2d_9 (Conv2D)	(None, 8, 8, 160)	384160
batch_normalization_9 (Batch	(None, 8, 8, 160)	640
re_lu_9 (ReLU)	(None, 8, 8, 160)	0
max_pooling2d_3 (MaxPooling2	(None, 4, 4, 160)	0
global_average_pooling2d (Gl	(None, 160)	0
flatten (Flatten)	(None, 160)	0
dense (Dense)	(None, 50)	8050
dropout (Dropout)	(None, 50)	0
dense_1 (Dense)	(None, 4)	204

Total params: 1,646,174
Trainable params: 1,643,998
Non-trainable params: 2,176

Figure 11: Model Summary Cont'd

A snapshot of the model summary is represented above. This shows some of the layers, shape, and number of parameters generated in each layer.

IV. Evaluation/Results

The choice of evaluation metrics for the proposed model were: Precision, Recall, F1-Score and Accuracy. These evaluation metrics are applied to the 4 categorical classes in the dataset. These metrics are discussed in the following part of this section. The acronyms tp, fp, tn, and fn refers to true positive, false positive, true negative, and false negative, respectively.

A. Precision

This is used to calculate the ratio of the predicted positive values (both true and false positive) that was also an actual positive value. It is calculated using the formula below:

$$\frac{tp}{tp + fp}$$

B. Recall

This is also referred to as sensitivity, calculates the ratio of the predicted positive of the total actual positive values. The formula for recall is shown below:

$$\frac{tp}{tp + fn}$$

C. F1-Score

F1-score or F-measure, is a value between 0 and 1 used to represent the harmonic mean between the precision and recall values. The F1-score is calculated as:

$$2 * \frac{p * r}{p + r}$$

D. *Accuracy*

Is one of the most used evaluation metrics; it is expressed as a ratio of the rightly predicted classes to the total number in the sample. The equation for accuracy is given as:

$$\frac{tp + tn}{tp + tn + fp + fn}$$

Table 2: Evaluation Metrics shows the values derived from the different chosen evaluation metrics for the proposed model. The model achieved an overall accuracy of 97% while the F1 scores for CNV, DME, drusen, and normal were 1.00, 0.94, 1.00, and 0.95, respectively. Based on the available metrics, it is safe to say that the model an overall acceptable performance in the detection of the above-mentioned eye defects. The recall, which is also referred to as sensitivity, describes the number of OCT images predicted to have an eye condition out of all the images with a form of eye defect. The Recall, Precision and F1 Score are all very important evaluation metrics due to the nature of the domain area.

Table 2: Evaluation Metrics

	Precision	**Recall**	**F1-Score**
CNV	1.00	0.97	0.98
DME	0.93	1.00	0.96
Drusen	0.99	1.00	1.00
Normal	1.00	0.94	0.97
Accuracy			**0.98**

The confusion matrix shown in Figure 12 shows a tabular layout of the performance of the model in terms of classification. The confusion matrix reveals that the model accurately predicts all the classifications of the CNV and Drusen eye defect but misclassified one of the DME defects as a normal OCT image.

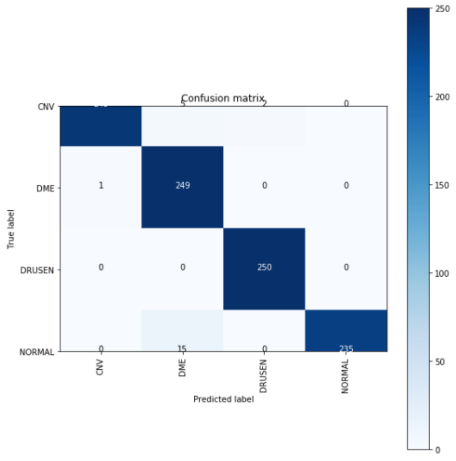

Figure 12: Confusion Matrix

V. Conclusion And Future Work

This paper discussed the application of CNN on the detection of CNV, DME, Drusen, and normal i.e. no defect in OCT images.

Majority of past work in this area focused on only the detection of one or the other eye defect. This project is one of few that focused on the detection of multiple eye defects. The model achieved an overall accuracy of 98% with an F1 score of 0.98, 0.96, 1.00, and 0.97 for CNV, DME, Drusen, and normal, respectively. A major advantage of the choice of CNN algorithm is that it takes the entire image as input, and automatically detects features that distinguish each class in the entire dataset as opposed to manually extracting the features in each class before training.

Owing to limited time and computation power, the model employed the use of down sampling which reduced the number of images in the majority classes to match the number of images in the minority class, as the number of images in the minority class was still sufficient for training the model. While this technique was applied to handle the issue of class imbalance in the dataset, the downside to this technique, however, is that there is risk of losing images with vital features which could be better used to describe the class. A more suitable approach, given more time, would be to apply down sampling = 0.5, which would reduce a smaller number of images from the majority class to avoid losing too much information from the said class.

References

[1] V. L. Tseng, P. B. Greenberg, I. U. Scott, and K. L. Anderson, 'Compliance with the American academy of ophthalmology preferred practice pattern for diabetic retinopathy in a resident ophthalmology clinic', *Retina*, vol. 30, no. 5, pp. 787–794, May 2010, doi: 10.1097/IAE.0b013e3181cd47a2.

[2] J. Kinyoun, F. Barton, M. Fisher, L. Hubbard, L. Aiello, and F. Ferris, 'Detection of Diabetic Macular Edema', *Ophthalmology*, vol. 96, no. 6, pp. 746–751, Jun. 1989, doi: 10.1016/S0161-6420(89)32814-4.

[3] H. E. Grossniklaus and W. R. Green, 'Choroidal neovascularization', *American Journal of Ophthalmology*, vol. 137, no. 3, pp. 496–503, Mar. 2004, doi: 10.1016/j.ajo.2003.09.042.

[4] T. A. Ciulla, A. G. Amador, and B. Zinman, 'Diabetic Retinopathy and Diabetic Macular Edema: Pathophysiology, screening, and novel therapies', *Diabetes Care*, vol. 26, no. 9, pp. 2653–2664, Sep. 2003, doi: 10.2337/diacare.26.9.2653.

[5] R. F. Spaide and C. A. Curcio, 'Drusen Characterization with Multimodal Imaging', *Retina*, vol. 30, no. 9, pp. 1441–1454, Oct. 2010, doi: 10.1097/IAE.0b013e3181ee5ce8.

[6] C. E. Baudoin, B. J. Lay, and J. C. Klein, 'Automatic detection of microaneurysms in diabetic fluorescein angiography', *Rev Epidemiol Sante Publique*, vol. 32, no. 3–4, pp. 254–261, 1984.

[7] G. G. Gardner, D. Keating, T. H. Williamson, and A. T. Elliott, 'Automatic detection of diabetic retinopathy using an artificial neural network: a screening tool.',

British Journal of Ophthalmology, vol. 80, no. 11, pp. 940–944, Nov. 1996, doi: 10.1136/bjo.80.11.940.

[8] R. Gargeya and T. Leng, 'Automated Identification of Diabetic Retinopathy Using Deep Learning', *Ophthalmology*, vol. 124, no. 7, pp. 962–969, Jul. 2017, doi: 10.1016/j.ophtha.2017.02.008.

[9] A. Osareh, B. Shadgar, and R. Markham, 'A Computational-Intelligence-Based Approach for Detection of Exudates in Diabetic Retinopathy Images', *IEEE Trans. Inform. Technol. Biomed.*, vol. 13, no. 4, pp. 535–545, Jul. 2009, doi: 10.1109/TITB.2008.2007493.

[10] Xiaohui Zhang and O. Chutatape, 'Top-Down and Bottom-Up Strategies in Lesion Detection of Background Diabetic Retinopathy', in *2005 IEEE Computer Society Conference on Computer Vision and Pattern Recognition (CVPR'05)*, San Diego, CA, USA, 2005, vol. 2, pp. 422–428, doi: 10.1109/CVPR.2005.346.

[11] Santhakumar R, M. Tandur, E. R. Rajkumar, Geetha K S, G. Haritz, and K. T. Rajamani, 'Machine learning algorithm for retinal image analysis', in *2016 IEEE Region 10 Conference (TENCON)*, Singapore, Nov. 2016, pp. 1236–1240, doi: 10.1109/TENCON.2016.7848208.

[12] A. Osareh, 'Automated identification of diabetic retinal exudates in digital colour images', *British Journal of Ophthalmology*, vol. 87, no. 10, pp. 1220–1223, Oct. 2003, doi: 10.1136/bjo.87.10.1220.

[13] D. Xiang *et al.*, 'Automatic Segmentation of Retinal Layer in OCT Images with Choroidal Neovascularization', *IEEE Trans. on Image Process.*, vol. 27, no. 12, pp. 5880–5891, Dec. 2018, doi: 10.1109/TIP.2018.2860255.

[14] M. García, C. I. Sánchez, M. I. López, D. Abásolo, and R. Hornero, 'Neural network based detection of hard exudates in retinal images', *Computer Methods and Programs in Biomedicine*, vol. 93, no. 1, pp. 9–19, Jan. 2009, doi: 10.1016/j.cmpb.2008.07.006.

[15] C. I. Sánchez, R. Hornero, M. I. López, M. Aboy, J. Poza, and D. Abásolo, 'A novel automatic image processing algorithm for detection of hard exudates based on retinal image analysis', *Medical Engineering & Physics*, vol. 30, no. 3, pp. 350–357, Apr. 2008, doi: 10.1016/j.medengphy.2007.04.010.

[16] J. H. Tan, U. R. Acharya, S. V. Bhandary, K. C. Chua, and S. Sivaprasad, 'Segmentation of optic disc, fovea and retinal vasculature using a single convolutional neural network', *Journal of Computational Science*, vol. 20, pp. 70–79, May 2017, doi: 10.1016/j.jocs.2017.02.006.

[17] U. Raghavendra, H. Fujita, S. V. Bhandary, A. Gudigar, J. H. Tan, and U. R. Acharya, 'Deep convolution neural network for accurate diagnosis of glaucoma using digital fundus images', *Information Sciences*, vol. 441, pp. 41–49, May 2018, doi: 10.1016/j.ins.2018.01.051.

[18] M. R. K. Mookiah, U. Rajendra Acharya, C. M. Lim, A. Petznick, and J. S. Suri, 'Data mining technique for automated diagnosis of glaucoma using higher order spectra and wavelet energy features', *Knowledge-Based Systems*, vol. 33, pp. 73–82, Sep. 2012, doi: 10.1016/j.knosys.2012.02.010.

[19] U. R. Acharya *et al.*, 'Decision support system for the glaucoma using Gabor transformation', *Biomedical Signal Processing and Control*, vol. 15, pp. 18–26, Jan. 2015, doi: 10.1016/j.bspc.2014.09.004.

[20] X. Chen, Y. Xu, D. W. Kee Wong, T. Y. Wong, and J. Liu, 'Glaucoma detection based on deep convolutional neural network', in *2015 37th Annual International Conference of the IEEE Engineering in Medicine and Biology Society (EMBC)*, Milan, Aug. 2015, pp. 715–718, doi: 10.1109/EMBC.2015.7318462.

[21] S. Simonthomas, N. Thulasi, and P. Asharaf, 'Automated diagnosis of glaucoma using Haralick texture features', in *International Conference on Information Communication and Embedded Systems (ICICES2014)*, Chennai, India, Feb. 2014, pp. 1–6, doi: 10.1109/ICICES.2014.7033743.

[22] F. Fink *et al.*, 'ICA analysis of retina images for glaucoma classification', in *2008 30th Annual International Conference of the IEEE Engineering in Medicine and Biology Society*, Vancouver, BC, Aug. 2008, pp. 4664–4667, doi: 10.1109/IEMBS.2008.4650253.

[23] U. R. Acharya, S. Bhat, J. E. W. Koh, S. V. Bhandary, and H. Adeli, 'A novel algorithm to detect glaucoma risk using texton and local configuration pattern features extracted from fundus images', *Computers in Biology and Medicine*, vol. 88, pp. 72–83, Sep. 2017, doi: 10.1016/j.compbiomed.2017.06.022.

[24] D. Kermany, 'Labeled Optical Coherence Tomography (OCT) and Chest X-Ray Images for Classification'. Mendeley, Jan. 06, 2018, doi: 10.17632/RSCBJBR9SJ.2.

[25] A. F. Agarap, 'Deep Learning using Rectified Linear Units (ReLU)', *arXiv:1803.08375 [cs, stat]*, Feb. 2019, Accessed: Aug. 16, 2020. [Online]. Available: http://arxiv.org/abs/1803.08375.